



Influence of Tb³⁺ doping on optoelectronic and crystallographic aspects of gadolinium-based BaSrGd₄O₈ nanophosphor for NUV-stimulated WLEDs

Shalini Kaushik¹, Suman Devi¹, Mukesh Kumar², Hina Dalal², Anamika Srivastava¹, Sanjay Gaur³, and Manish Srivastava^{1,*}

¹Department of Chemistry, Banasthali Vidyapith, Banasthali 304022, India

²Department of Chemistry, Maharshi Dayanand University, Rohtak 124001, India

³Department of Physics, GDC Memorial College, Bahal, Bhiwani 127028, India

Received: 14 June 2022

Accepted: 22 July 2022

Published online:
29 August 2022

© The Author(s), under exclusive licence to Springer Science+Business Media, LLC, part of Springer Nature 2022

ABSTRACT

Tb³⁺-activated gadolinium-based nanophosphor series was fabricated via a simple solution combustion (SC) methodology. Orthorhombic crystal lattice having space group Pnma (62) with irregularly shaped particles with sizes between 37 and 53 nm was formed. Morphological features were examined via transmission and scanning electron microscopic techniques (TEM and SEM). The elemental analysis was carried out through energy dispersive technology. On near-ultraviolet (NUV) stimulation, luminescence spectra presented a bright green emission at 546 nm wavelength corresponding to the electronic transition ⁵D₄ → ⁷F₅. The decay lifetimes, quantum efficiency, and non-radiative rates were also examined. The energy bandgap was examined via diffuse reflectance (DR) spectroscopy. The color coordinates lay in the greenish field, thus confirming their latent contention in phosphor-converted white light-emitting diodes (pc-WLEDs) and other advanced lighting applications.

1 Introduction

Nanotechnology, a new innovative technology, has been evolving as a fascinating target for material scientists due to its potential claims in the generation of white light-emitting diodes for solid-state lighting (SSL) purposes. These types of LEDs have more reimbursements than conventional incandescent lamps like less energy feeding, mercury less, an environment-friendly nature, and higher durability

[1, 2]. The conventional LEDs are mass-produced by incorporating Ce³⁺ ions in yellow garnet (YAG:Ce; Y_{3-x}Gd_xAl_{5-y}Ga_yO₁₂:Ce) at an excitation wavelength of 450–470 nm. But the red constituent in this type of LED is not sufficient, due to which their color temperature is lower [3]. Nowadays, as the global energy weights are growing, there is much necessity for such type of green energy capital. SSL technology plays a crucial role in this direction. To overcome the downsides of conventional LEDs, SSL technology

Address correspondence to E-mail: sagermanish1@gmail.com

includes one-step production of single-phase wLEDs and NUV-LEDs covered with RGB (Red–Green–Blue) phosphors having good color rendering index (CRI) and chromatic stability [4, 5].

A different proportion of RGB-based phosphors have been widely used with rare-earth-doped nanophosphors due to their durable spectra obtained in the visible region owing to the internal configuration changes between diverse f-states [6–13]. To make rare-earth-activated nanophosphor, the degree of occurrence of host matrices has been determined. Gadolinium-based host matrices form an imperative class of matriculants in inorganic chemistry due to the various structural alignments of the Gd–O unit. The current work has been done to develop a green-emitting series of Tb³⁺-doped BaSrGd₄O₈, phosphor for PC -WLED fabrication with good thermal strength. In reports formerly, Hina et al. blended and synthesized dysprosium-doped BaSrGd₄O₈ nanophosphor, with an effective heat dissipation solution-combustion approach and heat treatment of 1100 °C for 3 h [14]. There are many reports available for the UV source-excited nanophosphors for the fabrication of wLEDs and other SSL purposes e.g. Sangeeta et al. synthesized the color-tunable nanocrystalline SrGd₂Al₂O₇:Tb³⁺ phosphor for solid-s lighting applications having good luminescent properties of Tb³⁺ ions [15]. Heena et al. studied the luminescent properties of Tb³⁺-doped BaLa₂ZnO₅ nanoparticles for SSL and display technology [16]. Jyoti et al. studied the radiative rates of the multi-functional Ba₅Zn₄Y₈O₂₁:Tb³⁺ nanorods [17]. Sushma et al. studied the influence of Tb³⁺ doping on the structural and down-conversion luminescence behavior of SrLaAlO₄ nanophosphor for R-G-B-based white LEDs [18].

For the best information of the author; no report of optical behavior, atomic locations, or crystallographic treatment of the BaSrGd₄O₈:Tb³⁺ system was found. The stable crystal structure of BaSrGd₄O₈:Tb³⁺ nanophosphor is reached at 1100 °C for 3 h, which facilitates commercial production. White LEDs can be made by combining a near-ultraviolet LED or UV-LED with tricolor phosphor red, green, and blue (RGB). So, here we have selected Tb³⁺ ions as triggers to act as green components for the production of wLEDs. Among the numerous wet chemical approaches accessible for the production of nanophosphor, we have utilized the urea-aided SC approach as it is best known for its combination of

low temperature with virtuous consistency and better purity products [19]. In addition, X-ray diffraction (XRD) and optical analysis were performed and different optical and crystallographic features were studied.

2 Experimental

2.1 Phosphor fabrication

An effective SC technic was used to fabricate the series of Tb³⁺-doped BaSrGd₄O₈ nanophosphor. The precursors used in the fabrication of Tb³⁺-doped BaSrGd₄O₈ were barium nitrate, gadolinium nitrate, strontium nitrate, terbium nitrate, and urea with a purity of 99.99% (Sigma Aldrich). The stoichiometric values of all precursors are calculated from propellant chemistry using their oxidizing and reducing valancies. All the starting materials were dissolved in a minimal amount of deionized H₂O in a borosil tumbler and placed on a warm plate for approximately 8–12 min [12, 13]. The solution containing all the ingredients was then fired at 500 °C for 10–15 min. The radiant heat emission reaction occurs which increases the reaction temperature to 1400–1600 °C. Large volumes of gases such as N₂, CO₂, and H₂O vapor were also released and generated a solid powder which was then crushed and pulverized. The milled residue was then calcinated at 1100 °C for 3 h in the furnace and stored in a desiccator for more depiction. The schematic procedure to fabricate the above nanophosphor has been shown through a flow diagram in Fig. 1.

2.2 Characterizations executed

Phase investigation of synthetic nanoparticles was performed using powder X-ray diffraction (PXRD) performances recorded with a highly advanced and sophisticated diffractometer of Japan (Rigaku Ultima IV) and the standard technique of refinement, i.e. Rietveld refinement. The outlines of PXRD are documented in a range between 10° and 80° having a scan rate of 2°/min and scanning steps of 0.02°. To produce X-rays, CuK α radiation with a wavelength of 0.15405 nm, 40 mA (tube current), and 40 kV (tube voltage), were utilized to form the PXRD circuit. Chebyshev's modified function consisting of triple terms was cast-off to refine the background using the

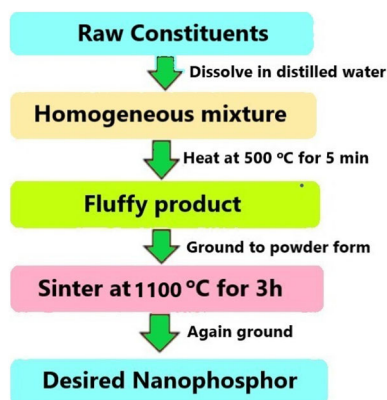


Fig. 1 A schematic flow diagram for the fabrication of Tb³⁺-doped BaSrGd₄O₈ nanophosphor

GSAS (General Structural Analysis System platform) [20–25].

Size and morphological aspects were analyzed using FEI TECNAI T20 S TWIN TEM (Thermofisher) and SEM (JEOL-JSM). The energy dispersive X-ray analysis i.e. EDAX (AMETEK) system evaluated the quantitative existence of numerous constituents in nano samples. Electrical power is maintained at 15 kV with 11 mm of operating distance. Longevity, color links, and photoluminescence properties were investigated using the Xe lamp spectrophotometer (Hitachi F-7000). It tracks the exciting and emission spectra, having photomultiplier tube (PMT) voltage (700 V), and the slit width (5 mm). DR spectroscopy was aided to study the energy gaps of the host lattice and doped nano sample.

3 Outcomes and discussion

3.1 Structural analysis

The crystalline structural study was accomplished with PXRD investigation and the resulting sample was found to be consistent with the typical host matrix framework provided by crystallographic information file (CIF) with # 1532345 (Fig. 2a). In addition, both the main matrix and the doped sample were purified using the Rietveld purification process to confirm the formation of orthorhombic phased nanocrystals. Table 1 covers a contrast between cell sizes of pure host matrix and doped nanocrystalline samples. The minor changes in crystal parameters confirm that the BaSrGd₄O₈ host matrix and doped BaSrGd_{3.8}Tb_{0.2}O₈ configuration share a similar

prototype. The distinct cell constraints after purification attained the values with $a = 10.3147 \text{ \AA}$, $b = 3.4973 \text{ \AA}$ and $c = 12.1631 \text{ \AA}$, V (volume of the cell) = 438.07 \AA^3 , $Z = 2$ and $\alpha = \beta = \gamma = 90^\circ$. The results of the Rietveld refinement over the host as well as doped optimal nanocrystals are shown in Fig. 2b and c. The measurement results of the latter are $\chi^2 = 1.621$, $R_p = 8.89\%$, and $wR_p = 9.78\%$. Table 1 shows a slight decline in the cell volume afterward inserting larger Gd³⁺ ions with somewhat smaller Tb³⁺ ions. This modification can also be supported by the declaration [26, 27]:

$$\Delta_r = \frac{R_m(\text{CN}) - R_d(\text{CN})}{R_m(\text{CN})} \times 100, \quad (1)$$

here CN mentions the coordination number of cations, R_m (CN) refers to the radiation of host cations, and R_d (CN) reports the effective ionic radius of doped cations. The Δ_r value of the Gd³⁺ and Tb³⁺ pair was 1.07%. This figure is less than 30% and is compatible with healthy alternatives [28–30]. Numerous refined parameters and relative occupancies of different elements present are collected in Table 2. The various lengths of the bonds formed and the crystallographic analysis of the fabricated samples were resolved by a software called ‘Diamond’ through the CIF file generated after refining. The various lengths of the bonds involved are concise in Table 3. The distinct sites of the prepared nanophosphor unit cell are highlighted in Fig. 2d along the c-axis showing that Gd³⁺/Tb³⁺ ions are bounded by six oxygen atoms with an octahedral space and Ba/Sr atoms form a square antiprismatic structure with oxygen atoms.

Additionally, the average extents of the made-up crystals were figured out as per Scherrer’s formulation [31, 32] as below:

$$D = \frac{0.941\lambda}{\beta \cos\theta}, \quad (2)$$

here D = mean crystallite dimension, λ informs about the X-Ray wavelength generated (0.1540 nm), β points towards the full width at half maxima (FWHM), and θ informs the diffraction angle. With these certain parameters, the mean extent of the manufactured nanocrystals was found 46 nm. Crystal size variation was also studied in Fig. 2e and found to increase with high dopant composition due to more agglomeration taking place at high concentrations.

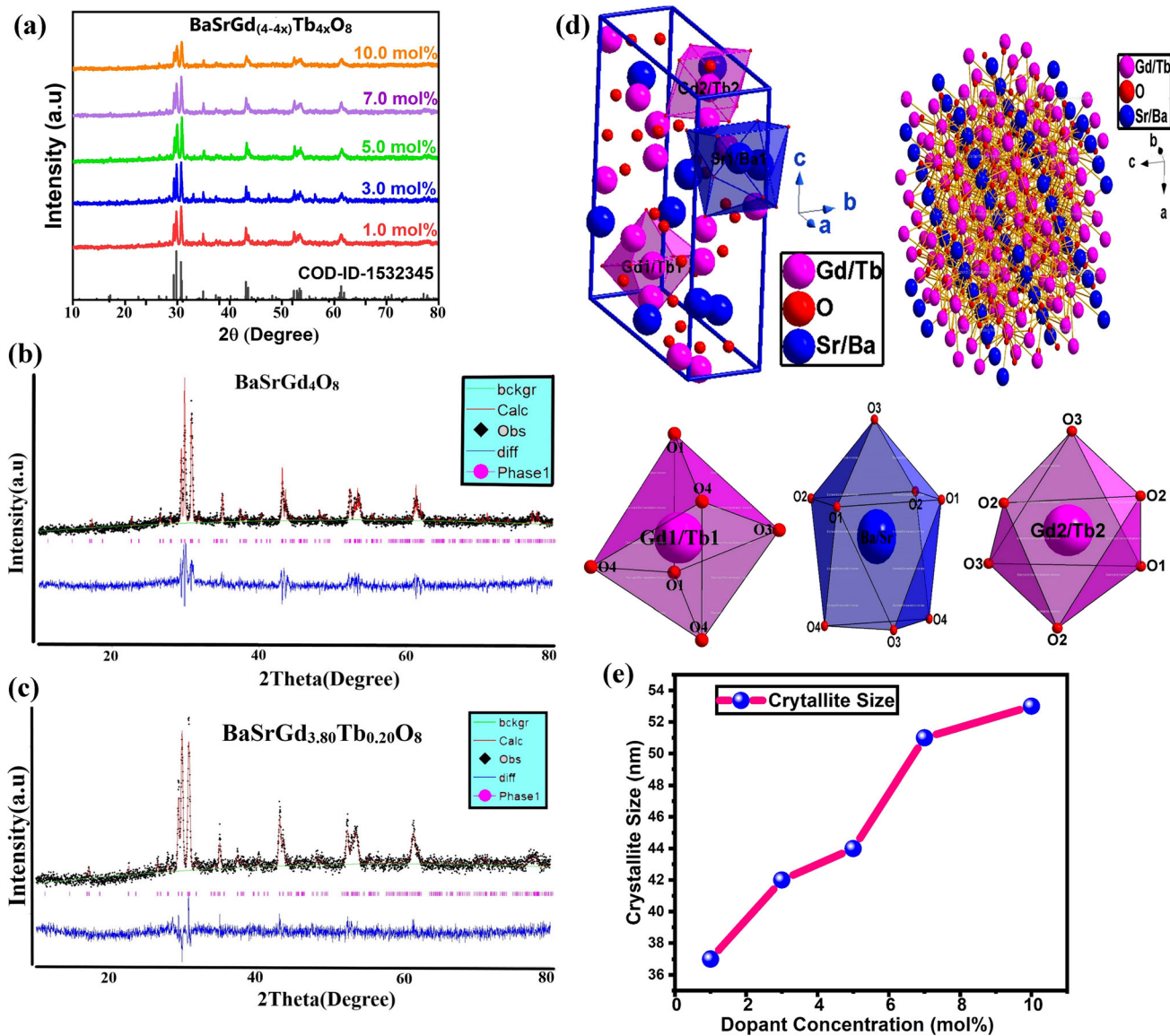


Fig. 2 a Combined PXRD patterns of BaSrGd_{4-4x}Tb_{4x}O₈ ($x = 1.0$ – 10.0 mol%) nanophosphor. b Rietveld refinement over host matrix BaSrGd₄O₈ yielding refined parameters of $wR_p = 10.05\%$, $R_p = 8.70\%$ and $\chi^2 = 1.525$. c Rietveld refinement over optimized nanophosphor BaSrGd_{3.8}Tb_{0.2}O₈ yielding refined parameters of $wR_p = 9.78\%$, $R_p = 8.89\%$ and

$\chi^2 = 1.621$. d Overall crystal structure of the optimized sample BaSrGd_{3.8}Tb_{0.2}O₈ along with coordination spheres of various types of atoms present. e Crystal size variation with dopant concentration for BaSrGd_{4-4x}Tb_{4x}O₈ ($x = 1.0$ – 10.0 mol%) nanophosphor

3.2 Morphological features

The crystallite size of BaSrGd_{3.8}Tb_{0.2}O₈ nanophosphor was also established by TEM examination (Fig. 3a) and originated to lie in the nano-range. Selective area electron diffraction (SAED) frameworks (Fig. 3b) have confirmed the crystallinity of nanophosphor due to the presence of concentric fringes and improved luminescence efficiency was

obtained. SEM micrograph of the optimal sample is shown in Fig. 3c to verify the hollow, cracked phase of the fixed sample caused by the combustion method of the solution. Basic quantitative research is done on an energy dispersive spectrum (EDS) map using the EDAX (AMETEK) platform. The EDS range of all elements is also documented in Fig. 3d and the basic map confirmed the existence of only Ba, Sr, Gd, Tb, and O elements (Fig. 3e).

Table 1 A comparison between crystal structure parameters of pure host matrix BaSrGd₄O₈ and optimized nanophosphor BaSrGd_{3.8}Tb_{0.2}O₈

Formula	BaSrGd ₄ O ₈	BaSrGd _{3.8} Tb _{0.2} O ₈
Formula weight (g mol ⁻¹)	122.74	122.80
Symmetry	Orthorhombic	Orthorhombic
Space group	Pnma (62)	Pnma (62)
<i>a</i> (Å)	10.3168	10.3147
<i>b</i> (Å)	3.4956	3.4973
<i>c</i> (Å)	12.1540	12.1631
<i>Z</i>	2	2
$\alpha = \beta = \gamma$ (degree)	90	90
Cell volume(Å ³)	438.31	438.07
Density (g cm ⁻³)	7.4398	7.4421
Pearson code	oP28	oP28
Formula type	NO2P4	NO2P4
Wyckoff sequence	c7	c7

3.3 Optical study

In the 200–800 nm wavelength domain, the UV-DR spectrum of the host matrix and optimal composition of nanocrystalline phosphor were documented and used to figure out the energy bandgap. Kubelka and Munk nominated a generalization to figure out the same as below [33–37]:

$$F(R_{\infty}) = \frac{(1 - R_{\infty})^2}{2R_{\infty}} = \frac{K}{S}, \quad (3)$$

$$hv = \frac{1240}{\lambda}, \quad (4)$$

here $F(R_{\infty})$ stands for the ‘Kubelka–Munk function’, S the scattering and K , the absorption coefficient, hv reports the single-photon energy, and λ the

Table 3 Various interatomic distances (Å) in the crystal structure of BaSrGd_{3.8}Tb_{0.2}O₈ nanomaterials

Bond type	Distance (Å)	Bond type	Distance(Å)
Gd1/Tb1-O3	2.2877(4) × 1	Gd2/Tb2-O3	2.2688(3) × 2
Gd1/Tb1-O1	2.3461(3) × 2	Gd2/Tb2-O1	2.2779(4) × 1
Gd1/Tb1-O4	2.3521(3) × 1	Gd2/Tb2-O2	2.3925(3) × 1
Gd1/Tb1-O4	2.3522(3) × 1	Gd2/Tb2-O2	2.3926(3) × 1
Gd2/Tb1-O4	2.3949(5) × 1	Gd2/Tb2-O3	2.2692(3) × 2
Gd2/Tb2-O2	2.3442(4) × 1	Gd1/Tb1-O3	2.2871(4) × 1
Gd2/Tb2-O2	2.3925(3) × 1	Gd2/Tb2-O3	2.2688(3) × 2
Gd2/Tb2-O2	2.3926(3) × 1	Gd2/Tb2-O1	2.2779(4) × 1
Gd2/Tb2-O3	2.2692(3) × 2	Gd2/Tb2-O2	2.3442(4) × 1
Gd1/Tb1-O3	2.2871(4) × 1	Gd2/Tb2-O2	2.3931(3) × 1

wavelength utilized. After this generalization, the energy bandgap was resolved as follows:

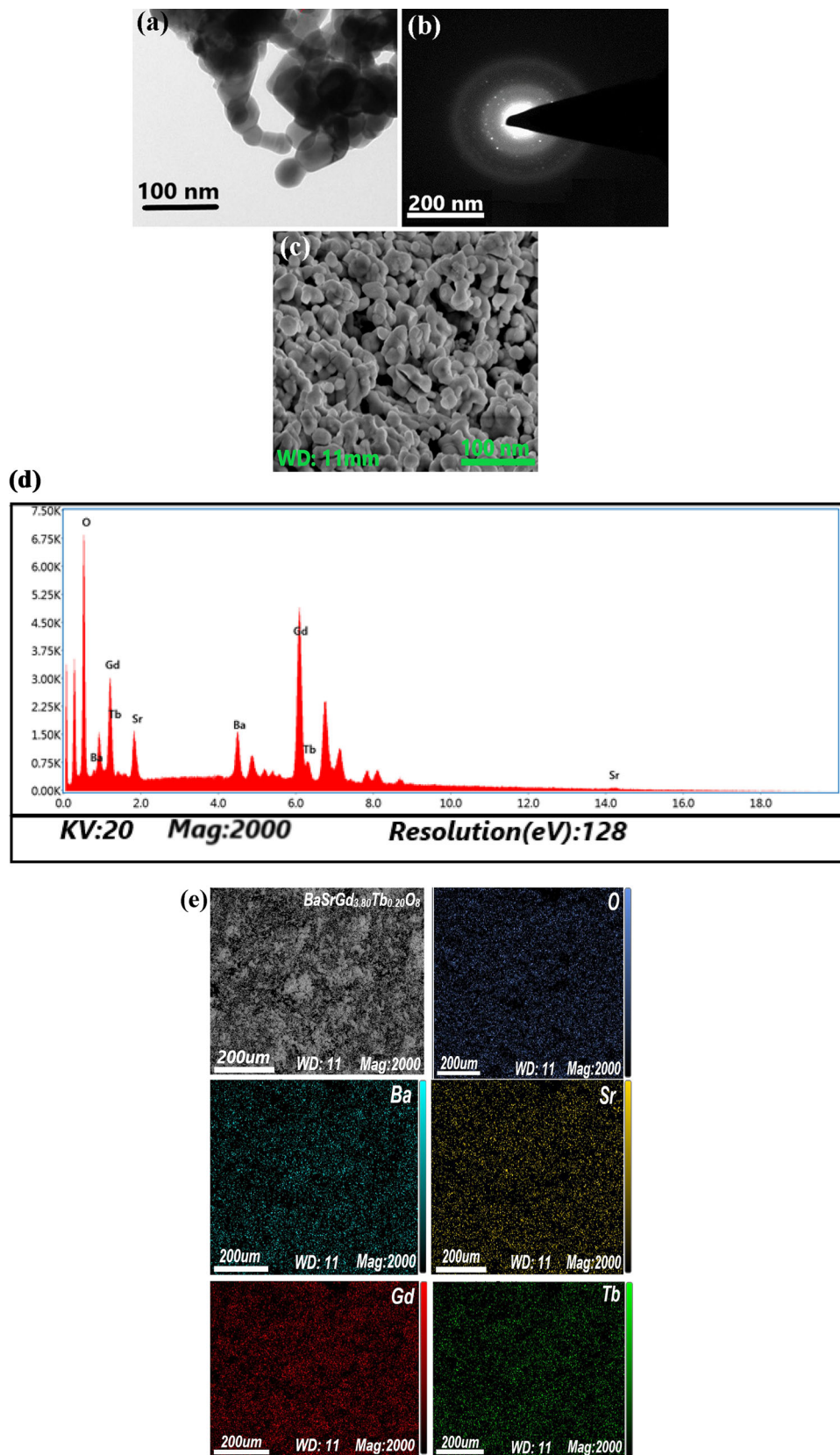
$$[F(R_{\infty})hv]^n = C(hv - E_g), \quad (5)$$

here C represents a constant term and the entity “ n ” has a static value of 0.5 for indirect permitted, 1.5 for direct inhibited, 2 for direct permitted, and 3 for indirect inhibited electronic translations. The x -axis tangent plot between $(\alpha hv)^2$ and hv for the host as well as optimized nanocrystal straight gives the $-$ bandgap value (Fig. 4a, b). The bandgap for the optimal sample was recorded at 5.10 eV and for the host matrix to be 5.27 eV [14]. These bandgap values are very similar to those of Wide Gap Semiconductors (WBG), which have subsequent effects on laser equipment, military radar, and wLEDs [38, 39]. A lesser bandgap value of the earlier is owing to the occurrence of a few additional electronic energy states assembling in the fabricated nanocrystals for fine light emission.

Table 2 Numerous refined atomic parameters and occupancies of BaSrGd_{3.8}Tb_{0.2}O₈ nanophosphor system

Label	Ion type	Wyck	Occupancy	<i>x/a</i>	<i>y/b</i>	<i>z/c</i>	<i>U</i> (Å ²)
Gd1	Gd ³⁺	4c	0.95	0.4209	1/4	0.6120	0.0000
Ba1	Ba ²⁺	4c	0.50	0.7514	1/4	0.6488	0.0000
O2	O ²⁻	4c	1.0	0.1215	1/4	0.4830	0.0000
Sr1	Sr ²⁺	4c	0.5	0.7514	1/4	0.6488	0.0000
O3	Ba ²⁺	4c	1.0	0.5050	1/4	0.7860	0.0000
Gd2	Gd ³⁺	4c	0.95	0.4236	1/4	0.1117	0.0000
O1	O ²⁻	4c	1.00	0.2140	1/4	0.1707	0.0000
O4	O ²⁻	4c	1.0	0.4300	1/4	0.4152	0.0000
Tb1	Tb ³⁺	4c	0.05	0.4209	1/4	0.6120	0.0000
Tb2	Tb ³⁺	4c	0.05	0.4236	1/4	0.1117	0.0000

Fig. 3 a–c respectively represent TEM, SAED, and SEM patterns of $\text{BaSrGd}_{3.8}\text{Tb}_{0.2}\text{O}_8$ nanophosphor representing the surface morphology and crystallinity of the prepared nanophosphor. **d** EDS spectrum of optimal nanophosphor $\text{BaSrGd}_{3.8}\text{Tb}_{0.2}\text{O}_8$. **e** Energy dispersive maps of all elements present in optimized-doped nanophosphor $\text{BaSrGd}_{3.8}\text{Tb}_{0.2}\text{O}_8$



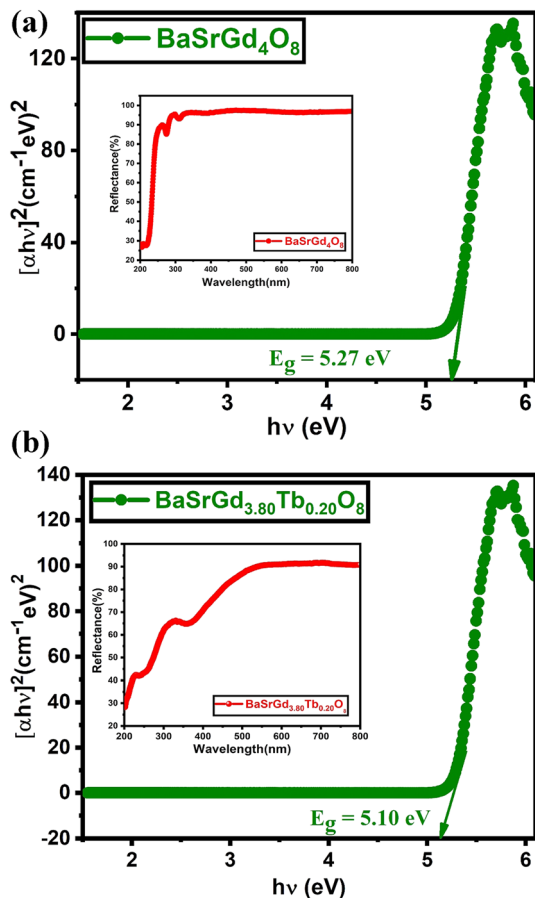


Fig. 4 **a** Tauc's plot to determine bandgap (E_g) for host matrix $\text{BaSrGd}_4\text{O}_8$ along with respective DR spectrum in the inset. **b** Tauc's plot to determine bandgap (E_g) for optimized nanophosphor $\text{BaSrGd}_{3.8}\text{Tb}_{0.2}\text{O}_8$ with corresponding DR spectrum in the inset

3.4 Luminous features

Small broadband centered at 240 nm is available in the excitation spectra of the Tb^{3+} -doped $\text{BaSrGd}_4\text{O}_8$ nanosample (Fig. 5a). This band occurs due to a charge transfer from O^{2-} to Tb^{3+} . Also, other maxima appear at 282, 312, 341, 368 nm emanating from ${}^5\text{D}_4 \rightarrow 5\text{d}$, ${}^7\text{F}_6 \rightarrow {}^5\text{H}_6$, ${}^7\text{F}_6 \rightarrow {}^5\text{L}_9$, and ${}^7\text{F}_6 \rightarrow {}^5\text{L}_{10}$ electronic transformations, which makes nanophosphor compatible with striking UV excited wLEDs. The excitation peak at 282 nm owing to the electronic transition from the ${}^5\text{D}_4 \rightarrow 5\text{d}$ state is the characteristic electronic transition of green emitter trivalent terbium ion, this time acting as an activator [40–43]. Therefore, the emission spectra (Fig. 5b) are documented utilizing this wavelength i.e. 282 nm in the 400–650 nm domain. Each specific energy conversion resembles an explicit wavelength, e.g. electronic

transition ${}^5\text{D}_3 \rightarrow {}^7\text{F}_5$ is at 412 nm, ${}^5\text{D}_3 \rightarrow {}^7\text{F}_4$ at 448 nm, ${}^5\text{D}_4 \rightarrow {}^7\text{F}_6$ at 490 nm, ${}^5\text{D}_4 \rightarrow {}^7\text{F}_5$ at 546 nm, ${}^5\text{D}_4 \rightarrow {}^7\text{F}_4$ at 591 nm, and ${}^5\text{D}_4 \rightarrow {}^7\text{F}_3$ at 625 nm. Among these, the utmost powerful transformation at 546 nm is attributed to ${}^5\text{D}_4 \rightarrow {}^7\text{F}_5$ electronic transition [44, 45]. Figure 5c describes the flow chart of the numerous energy stages along with different electronic conversions (also depicted in Table 4). The disparity between luminance power and activator composition was also examined in Fig. 5d. Note that the photoluminescent (PL) power first begins to upsurge up to 5.0 mol% and thereafter begins to decline. This decline in PL intensity owing to the concentration scavenging phenomenon due to non-radiant energy loss. There may many possible reasons for this, including radiation reabsorption, exchange interactions, and multipolar communications [46]. As no overlap was observed in the PL spectrum, so the possibility of radiation reabsorption is negligible. Critical distance plays a crucial role in deciding the character of energy exchange among activator ions that could happen only when the former does not exceed 4 Å. Blasse's formulation helps in this type of situation as follows [47–49]:

$$R_c = 2 \left[\frac{3V}{4\pi x_c N} \right]^{1/3}, \quad (6)$$

where x indicates the composition of the dopant with maximum PL intensity, V indicates the unit cell volume, and N indicates the cation numbers present in a single unit cell. With these constraints, R_c originated to be 10.5 Å which is higher than the critical distance permissible (5 Å) to implement the exchange process. Consequently, the most accepted concentration scavenging mechanism may be the d - d exchange, d - q , or q - q kind. The category of exchange, in this case, can be determined using Dexter's formula [50, 51]:

$$\log\left(\frac{I}{x}\right) = -\frac{s}{d} \log(x) + \log(f), \quad (7)$$

here I/x indicates the emanation intensity fraction of Tb^{3+} ions to the composition and d indicates the dimensions of the nanocrystalline sample, in this case, it is 3, and x stands for the composition of the trivalent erbium ions, superior to the optimal composition, and s represents a constant term having interaction values for qq , dq , and dd are 10, 8, and 6, correspondingly. The $\log(I/x)$ vs $\log(x)$ graph (Fig. 5e) shows a linear fit having a slope value of -1.7425 delivering a value of $s = 5.2275 \approx 6$. This is

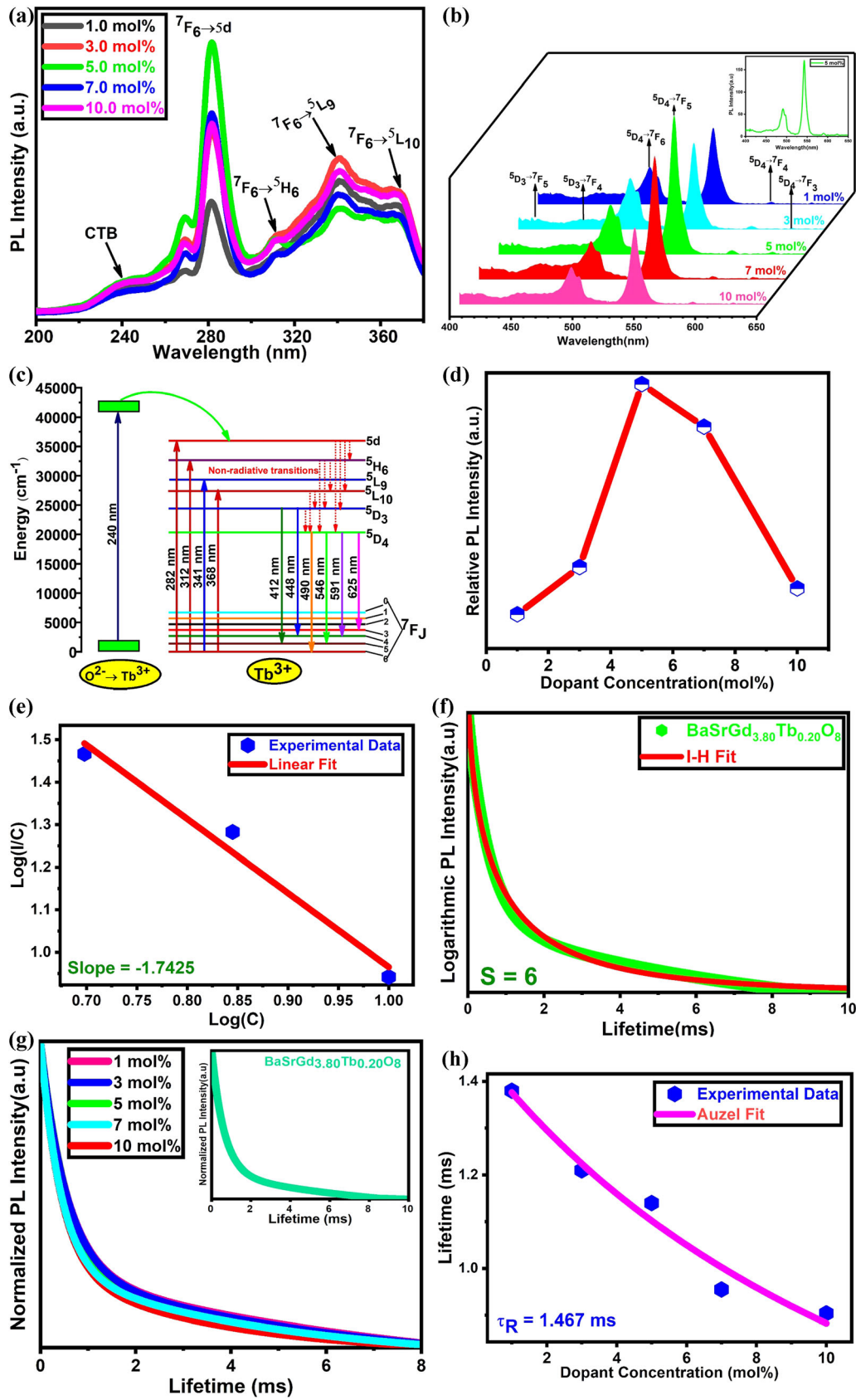


Fig. 5 **a** Combined PL excitation spectra of BaSrGd_{4-4x}Tb_{4x}O₈ ($x = 1.0$ – 10.0 mol%) nanophosphor recorded at $\lambda_{em} = 546$ nm. **b** Combined 3-D PL emission spectra of BaSrGd_{4-4x}Tb_{4x}O₈ ($x = 1.0$ – 10.0 mol%) nanophosphor recorded at $\lambda_{ex} = 282$ nm. **c** An elaborate energy level diagram presenting distinct electronic transitions in different energy levels for the terbium-doped BaSrGd₄O₈ nanophosphor. **d** Relation between PL emission intensity and concentration of dopant ions (mol%) for BaSrGd₄O₈:Tb³⁺ nanophosphor. **e** A linear variation between Log(I/x) and Log(x) in BaSrGd₄O₈: x Tb³⁺ ($x = 5.0$ – 10.0 mol%) nanophosphor. **f** Inokuti-Hirayama model fitted plot resulting in a value of $S = 6$ for optimized nanophosphor BaSrGd_{3.8}Tb_{0.2}O₈. **g** Lifetime decay curves of BaSrGd₄O₈: x Tb³⁺ ($x = 1.0$ – 10.0 mol%) nanophosphor recorded at $\lambda_{ex} = 282$ nm and $\lambda_{em} = 546$ nm. **h** Effect of Tb³⁺ composition on decay lifetime of the prepared nanophosphor using Auzel's method

the entity that confirmed the responsible $d-d$ exchange for concentration quenching. Further validation of the mechanism may be done using the simplification of the $I-H$ model. This indicates that two phenomena occur throughout the non-radiative energy transfer process: direct energy relocation (DET) and migration-assisted energy relocation (MAET). In this case, the DET precedes in the adjacent Er³⁺ ion, which could be resolved utilizing the decay data of lifetime [52].

$$(t) = I_0 \exp \left\{ -\frac{t}{\tau_0} - Q \left(\frac{t}{\tau_0} \right)^{\frac{3}{S}} \right\}. \quad (8)$$

In the given generalization, τ_0 , Q and t report lifetime decay of donor ions in absence of acceptor ions, energy relocation parameter, and lifetime decay correspondingly, so that

$$Q = \frac{4\pi}{3} \tau \left(1 - \frac{3}{S} \right) N_0 R_0^3, \quad (9)$$

here N_0 reports Tb³⁺ composition and R_0 the critical distance. $S = 6$ is best fitted in the $I-H$ plot (reported in Fig. 5f) confirming that the main cause for the quenching phenomenon is multipolar interactions.

The lifetime decay curves of the fabricated nanomaterials (Fig. 5g) were recorded at 282 nm (excitation) and 546 nm (emission) wavelengths. The lifetime decay curves show the mono-exponential performance characterized by the following generalization:

$$I = I_0 \exp \left(-\frac{t}{\tau} \right), \quad (10)$$

here τ , I , and I_0 characterize the lifetime decay and PL strength at time $t = 0$ and $t = t$, respectively. Table 5 sum up the evaluated values of decay lifetime from this generalization and shows that as the composition of the activator increases, it decreases from 1.3845 to 0.9046 ms. Quantum efficiency and non-radiative emission rates are also estimated and concise in Table 5. The non-radiative energy transfer rate may be resolved with the aid of the following simplification [53]:

$$\frac{1}{\tau_0} = \frac{1}{\tau_R} + A_{nR}, \quad (11)$$

where τ_0 and τ_R imply the observed and radiative lifetimes correspondingly. Auzel's method was aided to figure out τ_R (reported in Fig. 5h) as given [54] as follows:

Table 4 Distinct electronic transitions taking place in the spectrum of BaSrGd_{4(1-x)}Tb_xO₈ ($x = 1.0$ – 10.0 mol%) nanophosphors along with their intensity and position

Nanophosphor	Kind of spectrum	Transitions	Wavenumber (cm ⁻¹)	Intensity	
BaSrGd _{4(1-x)} Tb _x O ₈	Excitation at $\lambda_{em} = 546$ nm	O ²⁻ → Tb ³⁺	41667	Weak	
		⁷ F ₆ → 5d	35661	Very strong	
		⁷ F ₆ → ⁵ H ₆	32051	Medium	
		⁷ F ₆ → ⁵ L ₉	29325	Strong	
		⁷ F ₆ → ⁵ L ₁₀	27174	Strong	
		⁵ D ₃ → ⁷ F ₅	24272	Weak	
		Emission at $\lambda_{ex} = 282$ nm	⁵ D ₃ → ⁷ F ₄	22321	Weak
			⁵ D ₄ → ⁷ F ₆		
			⁵ D ₄ → ⁷ F ₅	20408	Strong
			⁵ D ₄ → ⁷ F ₄	18315	Very strong
$\lambda_{ex} = 282$ nm	⁵ D ₄ → ⁷ F ₃	16920	Weak		
$\lambda_{ex} = 282$ nm	⁵ D ₄ → ⁷ F ₃	16000	Very weak		

Table 5 CIE and CCT coordinates along with CCT values of BaSrGd_{4(1-x)}Tb_xO₈ (1–10 mol%) nano-crystalline phosphors

BaSrGd _{4(1-x)} Tb _x O ₈ (mol%)	CIE coordinates (x, y)	(u', v')	CCT (K)
1	0.3012, 0.4192	0.1625, 0.5070	6490.6
3	0.3127, 0.4303	0.1651, 0.5132	6101.3
5	0.3254, 0.4625	0.1643, 0.5265	5689.1
7	0.3103, 0.4207	0.1672, 0.5091	6191.2
10	0.2908, 0.4290	0.1534, 0.5109	6805.8

$$\tau(c) = \frac{\tau_R}{1 + \frac{c}{c_0} e^{-N/\beta}}, \tag{12}$$

here $\tau(c)$ indicates the lifetime at the composition “c”, N represents the phonon number, and c_0 represents a constant entity named concentration constant. The τ_R value was found 1.4670 ms on utilizing Auzel’s formulation. The proportion of the observed decay lifetime value to the radiation lifetime value simply estimates the quantum efficiency of the manufactured nano sample as below:

$$\varphi = \frac{\tau_0}{\tau_R}. \tag{13}$$

The internal quantum efficacy drops down with a rise in Tb³⁺ ions amount since the observed lifetime follows the same trend due to the transmission of energy amongst Tb³⁺ ions through a non-radiative path and is found to be 76.8% for the optimized sample.

3.5 Color chromaticity

The photoluminescence performance of the fabricated nanocrystalline samples was graphically confirmed by the International Commission de l’Eclairage (CIE), 1931 (Fig. 6a). The distinct color coordinates of the produced nanocrystals were figured out using the MATLAB database. All color combinations are found to lie in the greenish fragment of the chromaticity plot which expands the claimed zone in the SSL field e.g. NUV stimulated pc-wLEDs.

In addition, one more CIE constraint, color coordinate temperature (CCT), was detected using McCamy’s equation as given [55]:

$$CCT = -437n^3 + 3601n^2 - 6861n + 5514.31, \tag{14}$$

here n indicates the ratio of $(x - x_e)$ and $(y - y_e)$ (x and y report the coordinates of the prepared nanocrystals, x_e and y_e signify the epicenter coordinates), and u' and v' (CCT coordinates) are also obtained using the formulations:

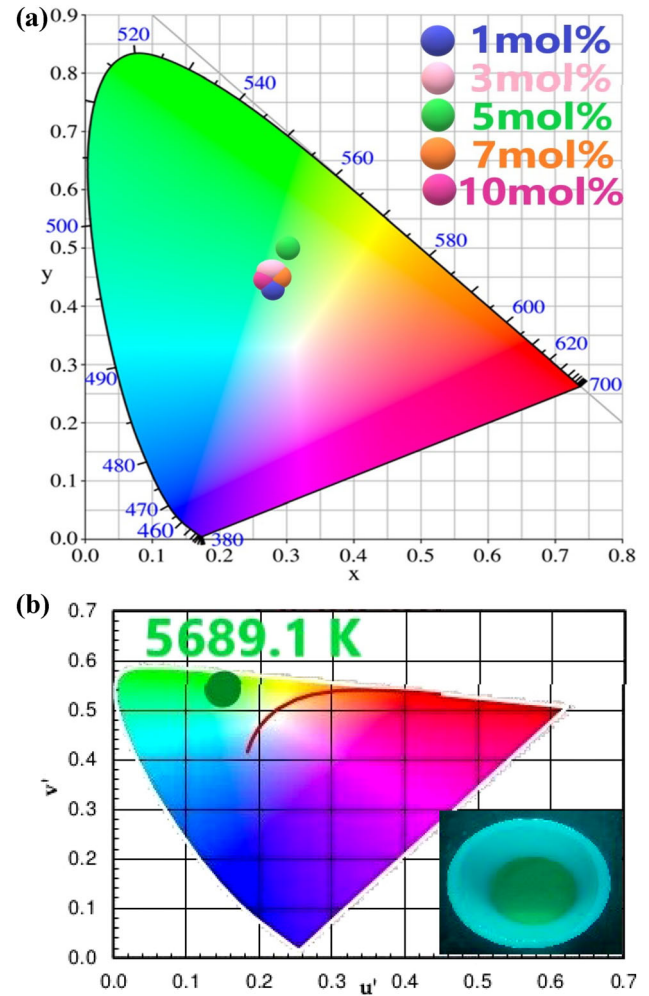


Fig. 6 **a** CIE chromaticity diagram of BaSrGd₄O₈:xTb³⁺ ($x = 1.0$ – 10.0 mol%) nanophosphor. **b** CCT coordinates (u' and v') and corresponding CCT value along with the digital image of the optimized nanophosphor BaSrGd_{3.8}Tb_{0.2}O₈ in the inset

$$u' = \frac{4x}{-2x + 12y + 3}, \tag{15}$$

$$v' = \frac{9y}{-2x + 12y + 3}. \tag{16}$$

Table 6 Photoluminescence lifetime, quantum efficiency and non-radiative rates for BaSrGd_{4(1-x)}Tb_xO₈ (1–10 mol%) nanophosphors

Tb ³⁺ concentration (mol%)	Lifetime (ms)	Quantum efficiency (%)	Non-radiative rates (s ⁻¹)
1	1.3845	93.6	40.6
3	1.2140	82.3	142.0
5	1.1425	76.8	193.6
7	0.9551	65.7	365.4
10	0.9046	61.2	423.8

Table 6 combinedly collects u' , v' , CIE, and CCT coordinates with respective CCT values. The optimal nano sample's CCT value was found 5689.1 K (shown in Fig. 6b). A digitized image of the optimized nanocrystalline powder has also been added in the inset of Fig. 6b.

4 Conclusions

Nanophosphors having a Pnma space group are made by an SC channel. Extensive research is being done on structural and photoluminescent features such as PXRD, EDAX, SEM, TEM, DR, PL, CIE, and CCT analysis. PXRD analysis confirmed the orthorhombic phase of the nano samples produced. Nano size and more surface features were investigated by SEM and TEM techniques. The EDAX technique was used to analyze the existence of different components in terms of volume. PL spectroscopy was used to study luminescence decay time, radiation conversion, non-radiative levels, and various intensity parameters. The luminescence power of the samples was found to reach a maximum of 5.0 mol%. The Quantum efficiency of the optimal sample was reported at 76.8% and the energy band-gap was found at 5.10 eV below the host matrix (5.27 eV) which ensures better doped nanophosphor light. CIE color links for all nano samples were present in the greenish section of the chromaticity map. The CCT value (5689.1 K) of the optimal sample also extends the active area of nanophosphor to the green-light emission that can also be used in the preparation of solid-state light and pc-wLED, etc.

Acknowledgements

The authors heartily acknowledge the Department of Chemistry, Banasthali Vidyapith, Banasthali to support this research work in every aspect.

Author contributions

SK and SD: data analysis, original draft writing, MK and HD: conceptualization and methodology, SG: review writing and data curation, AS and MS: results, discussion, and supervision.

Data availability

All the data analyzed in this research work are included in this article. If more supporting information is required it can be available on request from the corresponding author (Dr. Manish Srivastava).

Declarations

Conflict of interest The authors declare no competing interests.

References

- P. Pust, V. Weiler, C. Hecht, A. Tücks, A.S. Wochnik, A.-K. Henß, D. Wiechert, C. Scheu, P.J. Schmidt, W. Schnick, *Nat. Mater.* **13**, 891 (2014)
- M. Liu, W. Lü, J. Huo, B. Shao, Y. Feng, S. Zhao, H. You, *RSC Adv.* **6**, 92371 (2016)
- M. Dalal, V.B. Taxak, J. Dalal, A. Khatkar, S. Chahar, R. Devi, S.P. Khatkar, *J. Alloy Compd.* **698**, 662 (2017)
- J. Zhong, D. Chen, Y. Zhou, Z. Wan, M. Ding, W. Bai, Z. Ji, *Dalton Trans.* **45**, 4762 (2016)
- F. Baur, F. Glocker, T. Jüstel, *J. Mater. Chem. C* **3**, 2054 (2015)
- K.-S. Sohn, D.H. Park, S.H. Cho, J.S. Kwak, J.S. Kim, *Chem. Mater.* **18**, 1768 (2006)
- S. Zhang, B. Zhu, S. Zhou, J. Qiu, *J. Soc. Inf. Display* **17**, 507 (2009)
- P. Sehrawat, A. Khatkar, S. Devi, A. Hooda, S. Singh, R.K. Malik, S.P. Khatkar, V.B. Taxak, *Chem. Phys. Lett.* **737**, 136842 (2019)
- M. Sheoran, P. Sehrawat, N. Kumari, S.P. Khatkar, R.K. Malik, *Chem. Phys. Lett.* **773**, 138608 (2021)

10. P. Sehrawat, R.K. Malik, R. Punia, S. Maken, N. Kumari, Chem. Phys. Lett. **792**, 139399 (2022)
11. S. Chahar, M. Dalal, R. Devi, A. Khatkar, P. Boora, V.B. Taxak, S.P. Khatkar, J. Lumin. **199**, 442 (2018)
12. M. Dalal, V.B. Taxak, S. Chahar, J. Dalal, A. Khatkar, S.P. Khatkar, J. Alloy Compd. **686**, 366 (2016)
13. S. Devi, M. Dalal, J. Dalal, A. Hooda, A. Khatkar, V.B. Taxak, S.P. Khatkar, Ceram. Int. **45**, 7397 (2019)
14. H. Dalal, M. Kumar, P. Sehrawat, M. Sheoran, N. Sehrawat, S. Kumar, R.K. Malik, J. Mater. Sci.: Mater. Electron. **33**, 767 (2022)
15. S. Chahar, R. Devi, M. Dalal, M. Bala, J. Dalal, P. Boora, V.B. Taxak, R. Lather, S.P. Khatkar, Ceram. Int. **45**, 606 (2019)
16. H. Dahiya, M. Dalal, J. Dalal, V.B. Taxak, S.P. Khatkar, D. Kumar, Mater. Res. Bull. **99**, 86 (2018)
17. J. Dalal, M. Dalal, S. Devi, A. Hooda, A. Khatkar, R.K. Malik, V.B. Taxak, S.P. Khatkar, J. Mater. Sci.: Mater. Electron. **30**, 17547 (2019)
18. S. Devi, A. Khatkar, V.B. Taxak, A. Hooda, P. Sehrawat, S. Singh, S.P. Khatkar, J. Lumin. **221**, 117064 (2020)
19. R. Kumar Tamrakar, D.P. Bisen, K. Upadhyay, I.P. Sahu, M. Sahu, RSC Adv. **6**, 80797 (2016)
20. P. E. Stutzman and L. Struble, *Instructions in Using GSAS Rietveld Software for Quantitative X-Ray Diffraction Analysis of Portland Clinker and Cement* (National Institute of Standards and Technology, 2015), p. NIST TN 1884.
21. B.H. Toby, J. Appl. Crystallogr. **34**, 210 (2001)
22. L. Lutterotti, Nucl. Instrum. Methods Phys. Res. Sect. B **268**, 334 (2010)
23. A. C. Larson, R. B. Dreele, and B. Toby, **748**, (1994).
24. L. Lutterotti, M. Bortolotti, G. Ischia, I. Lonardelli, and H.-R. Wenk, in *Tenth European Powder Diffraction Conference*, edited by Deutsche Gesellschaft für Kristallographie (OLDENBOURG WISSENSCHAFTSVERLAG, 2007), pp. 125–130.
25. L. Lutterotti, D. Chateigner, S. Ferrari, J. Ricote, Thin Solid Films **450**, 34 (2004)
26. S. Devi, S. Kaushik, M. Kumar, H. Dalal, S. Gaur, S. Kumar, Appl. Phys. A **128**, 23 (2022)
27. H. Dalal, P. Sehrawat, M. Sheoran, M. Kumar, R.K. Malik, J. Mater. Sci.: Mater. Electron. (2021).
28. F.T.L. Muniz, M.A.R. Miranda, C. Morilla dos Santos, J.M. Sasaki, Acta Crystallogr. A **72**, 385 (2016)
29. K. Li, H. Lian, M. Shang, J. Lin, Dalton Trans. **44**, 20542 (2015)
30. M. Dhanalakshmi, H. Nagabhushana, S.C. Sharma, R.B. Basavaraj, G.P. Darshan, D. Kavyashree, Mater. Res. Bull. **102**, 235 (2018)
31. P. Kubelka, J. Opt. Soc. Am. **38**, 448 (1948)
32. A. Monshi, M.R. Foroughi, M.R. Monshi, WJNSE **02**, 154 (2012)
33. A.K. Vishwakarma, K. Jha, M. Jayasimhadri, B. Sivaiah, B. Gahtori, D. Haranath, Dalton Trans. **44**, 17166 (2015)
34. C. Yu, B. Chen, X. Zhang, X. Li, J. Zhang, S. Xu, H. Yu, J. Sun, Y. Cao, H. Xia, Phys. Chem. Chem. Phys. **22**, 7844 (2020)
35. Y. Zhang, B. Chen, S. Xu, X. Li, J. Zhang, J. Sun, X. Zhang, H. Xia, R. Hua, Phys. Chem. Chem. Phys. **20**, 15876 (2018)
36. H.A.N. Dharmagunawardhane, W.R. Woerner, Q. Wu, H. Huang, X. Chen, A. Orlov, P.G. Khalifah, J.B. Parise, J. Mater. Chem. A **2**, 19247 (2014)
37. Z. Fan, Z. Ye, Y. Qie, Y. Liu, Z. Shi, H. Yang, J. Alloy Compd. **817**, 152759 (2020)
38. H. Jain, S. Rajawat, and P. Agrawal, in *2008 International Conference on Recent Advances in Microwave Theory and Applications* (IEEE, Jaipur, Rajasthan, India, 2008), pp. 878–881.
39. P. Capper and S. Kasap, editors, *Springer Handbook of Electronic and Photonic Materials*, 2nd ed. 2017 (Springer International Publishing: Imprint: Springer, Cham, 2017).
40. M. Tian, P. Li, Z. Wang, X. Teng, Z. Li, J. Cheng, Y. Sun, C. Wang, Z. Yang, CrystEngComm **18**, 6934 (2016)
41. D. Geng, G. Li, M. Shang, C. Peng, Y. Zhang, Z. Cheng, J. Lin, Dalton Trans. **41**, 3078 (2012)
42. X. Li, Y. Zhang, D. Geng, J. Lian, G. Zhang, Z. Hou, J. Lin, J. Mater. Chem. C **2**, 9924 (2014)
43. A. Raja, G. Annadurai, D. Joseph Daniel, P. Ramasamy, J. Alloys Compds. **683**, 654 (2016).
44. D. Zhao, F.-X. Ma, Y.-C. Fan, L. Zhang, R.-J. Zhang, P.-G. Duan, Dalton Trans. **46**, 8673 (2017)
45. H. Liu, L. Liao, D. Yang, Q. Guo, L. Mei, Ceram. Int. **42**, 16579 (2016)
46. T. Grzyb, R.J. Wiglus, V. Nagirnyi, A. Kotlov, S. Lis, Dalton Trans. **43**, 6925 (2014)
47. G. Blasse, Phys. Lett. A **28**, 444 (1968)
48. Y. Zhai, X. Li, J. Liu, M. Jiang, J. Rare Earths **33**, 350 (2015)
49. M. Que, Z. Ci, Y. Wang, G. Zhu, S. Xin, Y. Shi, Q. Wang, CrystEngComm **15**, 6389 (2013)
50. H.S. Yogananda, R.B. Basavaraj, G.P. Darshan, B. Daruka Prasad, R. Naik, S.C. Sharma, H. Nagabhushana, J. Colloid Interface Sci. **528**, 443 (2018)
51. R.G. Abhilash Kumar, S. Hata, K. Ikeda, K.G. Gopchandran, Ceram. Int. **41**, 6037 (2015)
52. T. Manohar, S.C. Prashantha, R. Naik, H. Nagabhushana, H.P. Nagaswarupa, K.S. Anantharaju, K.M. Girish, H.B. Premkumar, Sens. Actuators B **243**, 1057 (2017)

53. A.A. Christy, O.M. Kvalheim, R.A. Velapoldi, *Vib. Spectrosc.* **9**, 19 (1995)
54. F. Auzel, *J. Lumin.* **100**, 125 (2002)
55. C.S. McCamy, *Color Res. Appl.* **17**, 142 (1992)

Publisher's Note Springer Nature remains neutral with regard to jurisdictional claims in published maps and institutional affiliations.

Springer Nature or its licensor holds exclusive rights to this article under a publishing agreement with the author(s) or other rightsholder(s); author self-archiving of the accepted manuscript version of this article is solely governed by the terms of such publishing agreement and applicable law.